

---

# Modeling Laser–Plasma Interaction Physics Under Direct-Drive Inertial Confinement Fusion Conditions

## Introduction

Laser–plasma interaction (LPI) processes taking place in indirect- and direct-drive targets differ significantly in several ways. Plasma electron densities  $n_e$  in hohlraum targets are typically a few percent of the critical density  $n_c = m_e \omega_0^2 / 4\pi e^2$ , so that the main instability mechanisms are stimulated Raman and stimulated Brillouin scattering (SRS and SBS, respectively), which typically have very large predicted linear gains due to the long scale lengths of near-uniform plasma.<sup>1</sup> The theoretical challenge here is to understand the nonlinear saturation mechanisms that are responsible for the small, observed reflectivities. In direct-drive targets the plasma is inhomogeneous, with the linear gain for parametric instabilities often limited by the inhomogeneity of the plasma, rather than by damping of the unstable waves. In direct-drive targets, all electron densities up to critical ( $n_e \sim 8 \times 10^{21} \text{ cm}^{-3}$  for 0.351- $\mu\text{m}$  light) can be accessed by the laser. As a consequence of the dispersion relations of the participating waves, SBS can take place anywhere in the underdense region  $n_e < n_c$ , and SRS can take place anywhere below the quarter-critical surface  $n_e \leq n_c/4$ . At the quarter-critical surface SRS is in competition with two-plasmon decay (TPD), a particularly dangerous instability because of its low threshold and its ability to produce hot electrons that preheat the target. Complicated physics is expected at the critical surface itself, including but not limited to resonance absorption, profile modification, instability, and surface rippling.<sup>2</sup> Interactions in the underdense plasma corona are further complicated by the crossing of multiple beams. These beams can interact parametrically via common decay waves, excited simultaneously by several beams, or via electromagnetic seeding involving specular or parametric reflections at or near the critical-density surface. The need to take into account such complications means that simple theoretical models are of rather limited use. One must adopt multidimensional simulation tools that are able to model the necessary physical processes on a large scale in order to have a hope of interpreting current experimental data and making predictions for future experiments.

While modeling LPI in *indirect-drive*-relevant plasmas has received a great deal of attention, and several semipredictive simulation codes have been developed,<sup>3,4–6</sup> the same cannot be said for direct drive. Recently pF3D, a three-dimensional, parallel LPI interaction code developed by LLNL, has been modified at LLE for use in direct-drive conditions. The significant advantage of pF3D<sup>3</sup> over the code *HARMONHY*<sup>4</sup> is its efficient parallelization using message passing, which has been exploited using Hydra, a 64-processor SGI Origin. This article describes recent developments in this regard, and in addition to some background on pF3D and similar codes, shows some of the first results that have modeled long-scale-length OMEGA multibeam experiments.

This article is organized as follows: The next section gives the background behind the modeling of large-scale LPI experiments and includes a discussion of the physical effects that make such simulations especially challenging. The section on **Simulations** gives details specific to the simulation of OMEGA experiments, including the treatment of the expanding plasma, the critical surface, and collisional absorption. It also contains the first pF3D results in direct-drive geometry, including simulations of SBS backscatter for a range of laser intensities. Simulations exhibiting self-smoothing of laser light are also presented. The final section explains the relevance of these simulations not only to present, but also to future OMEGA and National Ignition Facility (NIF) experiments. Further advances expected in the near future are also explored.

## The Physics of Large-Scale Modeling

One of the reasons for the complexity of LPI, and indeed plasma physics in general, is the mixing between disparate length scales. In LPI, the plasma response at scales around a fraction of the laser wavelength  $\lambda_0$  is generally not independent of those taking place at the much larger hydrodynamic scale length of the target,  $l_h$ . For NIF-scale targets irradiated by 0.351- $\mu\text{m}$  light, this ratio can be very large:

$l_h/\lambda_0 \sim 10^3$  to  $10^4$  (an example of this is the onset of large-scale flow due to SBS momentum deposition<sup>7</sup>). In recent years one advance in simulations that has made large-scale simulations possible has been the use of wave-envelope methods<sup>3,4,8</sup> that attempt to surmount these problems.

Another major complication for LPI is the complexity of the plasma response. Typical experimental scales of interest to laser fusion (both direct and indirect drive) are lengths of the order of 1 mm and times of 1 ns. It is quite impossible to model the plasma over these scales using any first principles model, such as particle-in-cell (PIC), Vlasov, or Fokker-Planck. One must necessarily deal with a reduced description, the simplest being the plasma fluid, where the only information retained from the single particle distribution function is its hydrodynamic moments. Although fluid models are the simplest (though still containing a host of nonlinearities), one cannot often neglect linear and nonlinear kinetic effects. Advances have been made in combining both linear wave-particle interaction (Landau damping),<sup>9</sup> electron kinetic effects such as nonlocal electron transport,<sup>4</sup> and nonlinear frequency shifts<sup>10</sup> into fluid codes.

### 1. Wave-Envelope Methods and the Paraxial Approximation

The basic idea in wave-envelope methods is to take advantage of the fact that it is often possible to write the transverse electric field of the laser as a sum of components that are each well characterized by a given frequency and wave number and also well separated from one another (spectrally). By enveloping around, and hence explicitly removing, the characteristic spatial and temporal frequency of each component, one arrives at equations where only the slow variation of the envelope needs to be followed. This leads to a relaxation of numerical constraints, coarser grids, and larger simulation volumes. An example of this is the paraxial approximation where one needs only to resolve the Rayleigh length and not the wavelength of the light. In the paraxial approximation, the constraint that the envelope function be slowly varying in space restricts the model to describe only light propagating within a range of wave numbers and frequencies not too far from the characteristic frequencies. Experience shows that an angular  $\pm 30^\circ$  can be tolerated, but this is often good enough for practical purposes.<sup>11</sup> Complications are that the plasma responds to the ponderomotive force and ohmic heating, which are quadratic in the electric field. Hence there are ponderomotive and thermal sources at the beat frequencies, both spatial and temporal, of all the transverse components. To retain the advantage, the plasma response must likewise be harmonically decomposed around each frequency present, taking into ac-

count nonlinear couplings between each,<sup>7</sup> as is done in both pF3D<sup>3</sup> and *HARMONHY*,<sup>4</sup> i.e., it is through the plasma response that the transverse electromagnetic components are nonlinearly coupled.

To make these general statements more concrete, we will describe how the above procedure applies to SBS (both near-backward and near-forward) in the simulation codes pF3D and *HARMONHY* (although the algorithms differ between the two codes, the general approach is essentially the same in each). Raman scattering can be treated in a similar way, but for simplicity we will consider only Brillouin here. Consider a transverse electromagnetic wave characterized by its amplitude  $\tilde{\mathbf{E}}$ . The time-enveloped amplitude  $\mathbf{E}$  is defined by the equation  $\tilde{\mathbf{E}} = \mathbf{E} \exp(-i\omega_0 t) + \text{c.c.}$ , and it satisfies the time-enveloped Maxwell equation:

$$\left\{ 2i\partial_t + \frac{c^2}{\omega_0} \nabla^2 + \omega_0 \left[ 1 - \frac{n_e}{N_c} (1 - i\nu_{ei}/\omega_0) \right] \right\} \mathbf{E} = 0, \quad (1)$$

where  $\mathbf{E}$  is assumed to vary on time scales much greater than  $\omega_0^{-1}$ . We have ignored here the term proportional to  $\nabla(\nabla \cdot \mathbf{E})$ , but we have retained the damping of electromagnetic waves, usually neglected in underdense plasma, since it is important close to the critical surface in direct-drive plasmas. Motivated by physical arguments, we expect the electric field to contain two spectral features, one corresponding to transverse waves propagating in the general direction of the laser axis and another propagating in the near-backward direction (SBS in the underdense region is expected to be reasonably well collimated in the backward direction as the longitudinal correlation length of the laser is greater than in the transverse direction by a large multiple of the  $f$  number). Hence, we write

$$\begin{aligned} \mathbf{E}(\mathbf{x}, t) = & \mathbf{E}_+(\mathbf{x}, t) \exp \left[ i \int_0^z k_0(z') dz' \right] \\ & + \mathbf{E}_-(\mathbf{x}, t) \exp \left[ i \int_z^L k_0(z') dz' \right]. \end{aligned} \quad (2)$$

Here the axially dependent wave number  $k_0(z)$  must satisfy the linear dispersion relation for transverse waves  $k_0(z) = \omega_0/c \sqrt{1 - N_{e,\text{sec}}/N_c}$ , and the electron density  $N_{e,\text{sec}}$  is defined later in Eqs. (4) and (6). The slowly varying envelopes then satisfy the equations

$$\begin{aligned} & \left( \partial_t + V_g \partial_z + \frac{1}{2} \partial_z V_g + \frac{v_{ei}}{2} \right) \mathbf{E}_+ - \frac{ic^2}{2\omega_0} \left( \varepsilon_{\text{par}} \partial_z^2 + \nabla_{\perp}^2 \right) \mathbf{E}_+ \\ & = -i \frac{\omega_0}{2N_c} (n_0 \mathbf{E}_+ + n_1 \mathbf{E}_-), \end{aligned} \quad (3a)$$

$$\begin{aligned} & \left( \partial_t - V_g \partial_z - \frac{1}{2} \partial_z V_g + \frac{v_{ei}}{2} \right) \mathbf{E}_- - \frac{ic^2}{2\omega_0} \left( \varepsilon_{\text{par}} \partial_z^2 + \nabla_{\perp}^2 \right) \mathbf{E}_- \\ & = -i \frac{\omega_0}{2N_c} (n_0 \mathbf{E}_- + n_1^* \mathbf{E}_+), \end{aligned} \quad (3b)$$

where  $V_g = c^2 k_0(z)/\omega_0$  is the magnitude of the group velocity of the light and  $v_{ei} = 4/3\sqrt{2\pi} \ln \lambda e^4 Z n_e m_e^{-1/2} T_e^{-3/2}$  is the electron-ion collision frequency, which is responsible for the collisional damping of the electromagnetic waves. The parameter  $\varepsilon_{\text{par}}$  has been introduced, and it takes on the values  $\varepsilon_{\text{par}} = 0$  or  $1$ , corresponding to the paraxial approximation and the unapproximated wave equation, respectively. Notice that the paraxial approximation assumes that  $\partial/\partial z \ll k_0$ .

## 2. Plasma Response

The presence of the high-frequency beat terms between  $E_+$  and  $E_-$  in the ponderomotive force,

$$F_{\text{pond}} = \nabla U = e^2 / (4m_e \omega_0^2) \nabla |\mathbf{E}|^2,$$

motivates a decomposition of all the fluid variables in the same fashion as outlined here for the electron density  $n_e$ :

$$n_e = N_0 + [n_1 \exp i\psi(z) + \text{c.c.}]. \quad (4)$$

In this decomposition,  $n_1$  is the (complex) amplitude of the ion-acoustic wave (IAW) driven by the backward SBS process, whose phase  $\psi(z)$  is given by

$$\psi(z) = \int_0^z k_0(z') dz' - \int_z^L k_0(z') dz',$$

so that  $\partial_z \psi(z) = k_{\text{IAW}}(z)$ , where  $k_{\text{IAW}} = 2k_0$  denotes the local wave number of the SBS-driven IAW. The amplitude satisfies

$$\begin{aligned} & \left( \frac{d}{dt} + 2ik_0 u_z + v_{\text{ia}} \right)^2 n_1 + \left( \omega_a - 2ik_0 C_a^2 \frac{\partial}{\partial z} - C_a^2 \nabla^2 \right) n_1 \\ & = -k_0^2 \frac{Z m_e}{m_i} N_0 E_+ E_-^* + S_a, \end{aligned} \quad (5)$$

where

$$d/dt = \partial/\partial t + \mathbf{u} \cdot \nabla$$

is the convective derivative,  $C_a = \sqrt{(Z T_e + 3 T_i)/m_i}$  is the IAW sound speed,  $v_{\text{ia}}$  is the ion-acoustic damping rate, and  $S_a$  is the thermal Cherenkov source of ion waves. (We have changed the notation slightly from Ref. 3.) In Eq. (4),  $N_0$  denotes the slowly varying part of the electron density for which the quasi-neutral limit is correct. For use in Eqs. (3), the slowly varying part  $N_0$  must itself be decomposed into a sum of a secular piece,  $N_{e,\text{sec}}$ , and a quasi-static, large-scale perturbation  $n_0$ ,

$$N_0 = N_{e,\text{sec}} + n_0. \quad (6)$$

The secular piece of the background equilibrium electron density is the part that varies over the interaction region, due to hydrodynamic expansion of the target, and whose phase has been taken into account by allowing  $k_0$  to be a function of  $z$  in the usual WKB (Wentzel, Kramers, Brillouin) manner. Its value at a particular axial location is equal to the transverse spatial average of  $N_0$ . The quasi-static, large-scale perturbation  $n_0$  is related to flow generation caused by momentum transfer, self-focusing/filamentation, and forward-scattering processes.

The slowly varying plasma-hydrodynamic quantities satisfy a nonlinear set of equations,

$$\partial_t \rho + \nabla \cdot (\rho \mathbf{u}_i) = 0, \quad (7a)$$

$$\begin{aligned} & \partial_t (\rho \mathbf{u}_i) + \nabla \cdot (\rho \mathbf{u}_i \mathbf{u}_i) \\ & = -\nabla (P_i + P_e) - \langle \rho \nabla U \rangle_0 - 2v_{Fp} \rho \mathbf{u}_i, \end{aligned} \quad (7b)$$

$$\frac{3}{2}[\partial_t P_i + \nabla \cdot (\mathbf{u}_i P_i)] + P_i \cdot \mathbf{u}_i = \nabla_{\perp} \cdot (\kappa_i \nabla_{\perp} T_i) + Q_i, \quad (7c)$$

$$\begin{aligned} & \frac{3}{2}[\partial_t \delta T_e + \nabla \cdot (\mathbf{u}_i \delta T_e)] + \delta T_e \nabla \cdot \mathbf{u}_i \\ & = \nabla_{\perp} \cdot (\kappa_{e,NL} \nabla_{\perp} T_e) + Q_e. \end{aligned} \quad (7d)$$

Here,  $\rho = m_i N_0 / Z$  is the ion mass density,  $Z$  is the average ion charge,  $P_e = N_0 T_e$  and  $P_i = (\rho / m_i) T_i$  are the electron and ion pressures, respectively,  $Q_e$  and  $Q_i$  are the electron and ion heating rates,  $\kappa_i$  and  $\kappa_{e,NL}$  are the ion and (possibly nonlocal) electron thermal conductivities, and the quantity  $\nu_F$  denotes the damping operator describing Landau damping and ion-ion collisions (see Ref. 12).

Most efforts have concentrated on hohlraum conditions, where no critical surface is present, but we are now applying pF3D, solving Eqs. (3), (5), and (7) to OMEGA direct-drive experiments.

### Simulations of Long-Scale-Length OMEGA Experiments

Experimental OMEGA campaigns have addressed LPI conditions that closely resemble NIF direct-drive ignition targets at the start of the main pulse using single, staggered multiple-beam irradiation of solid, planar CH targets. Full-aperture backscatter stations (FABS) have measured the time-integrated, time-resolved SBS as well as SRS backscatter energy and spectra. In the present work, we discuss SBS and make comments about TPD only. In general terms, the level of observed SBS backscatter for single-beam, normal incidence increases exponentially with laser intensity up to intensities of about  $2 \times 10^{14}$  W/cm<sup>2</sup>, with corresponding reflectivities of ~1%, after which it begins to saturate with reflectivities greater than, or around, 10%. This level can be reduced significantly by the addition of SSD (smoothing by spectral dispersion) bandwidth (0.5 or 1 THz experimentally) and by polarization smoothing (PS), both of which seem to be more efficient at removing the frequency upshifted (blue) part of the backscattered spectrum than the downshifted (red), and leads to reflectivities of a fraction of a percent. Similar behavior is also seen in the case of multiple-beam irradiation.

The SBS spectra (features near  $\lambda_0 \sim 351$  nm) consistently show two distinct features. One feature (referred to as the

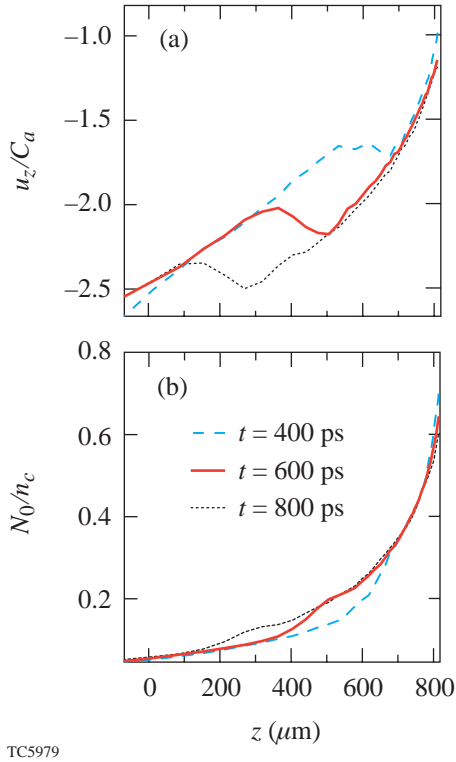
“blue feature”) has a shift to shorter wavelengths that increases in time up to a maximum experimentally observed spectral shift of  $\delta\lambda = \lambda_0^2 / (2\pi c) \delta\omega \sim 1$  nm. This is due to SBS in the underdense plasma corona where the flow velocity due to target expansion is supersonic and  $|\mathbf{u}_i| > C_a$ . The other spectral feature is shifted to longer wavelengths (the “red feature”) and is seen predominantly in the specular direction, i.e., if the beam is not normally incident and there is no opposing beam that could specularly reflect light into the FABS, then this feature is absent. This feature must arise from interactions very close (tens of microns) to the critical surface and is presumably seeded by specular reflection. The blue component is observed only in the backscatter direction and is seen regardless of the angle between the laser axis and the target normal. The temporal duration of the blue feature also differs between multibeam and single-beam irradiation, but this is likely due to the different hydrodynamics between the two targets. It then seems that the two spectral features have their origins in two well-separated regions in the plasma. Based on the expected hydrodynamic profile, from *SAGE* simulations,<sup>13</sup> the red feature must come from a region separated by only tens of microns from the critical surface, whereas the blue feature comes from a region hundreds of microns out into the corona. The critical region is not currently modeled in a self-consistent manner in pF3D and will not be addressed in detail here. (The actual details on how the critical surface is presently treated will be detailed below.) Work is under way to study this region separately using a full-wave code that does not assume the paraxial approximation and uses the pF3D simulations to provide the necessary boundary conditions.

Detailed understanding of the experiment is necessary for confident predictions and future NIF/OMEGA experiments. Before proceeding with our simulations relevant to the current OMEGA experiments, we will discuss in detail the modeling of both the inhomogeneous plasma profile and the critical surface.

#### 1. Modeling the Hydrodynamic Expansion of the Target

Hydrodynamic evolution of the target during the nanosecond laser pulse is significant, and previous experience with experiments conducted at LULI has shown that this must be modeled accurately for close agreement with experimental data.<sup>14</sup> The predictive value of *SAGE* has been verified over several experimental campaigns, so we have chosen to initialize our plasma hydrodynamics using data provided by *SAGE*. Figure 91.1 shows the initial conditions, taken from *SAGE*, corresponding to the  $z$  component of the expansion velocity  $\mathbf{u}_i$  and the plasma electron density  $N_0$  for various times relative

to the start of the interaction pulse. This flow velocity gives a spatially dependent Doppler shift to IAW, and its gradient localizes the three-wave SBS interaction, which are all essential features of the experiment.



TC5979

Figure 91.1

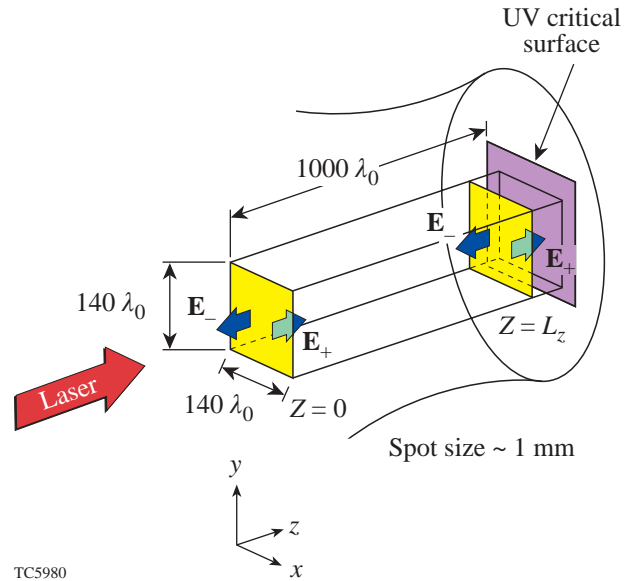
The component of the plasma expansion velocity (normalized to  $C_a$  for hydrogen at 1 keV) in the direction of the target normal, and electron plasma density as a function of the axial coordinate  $z$ . The gradient in the expansion velocity limits the resonance region for backward stimulated Brillouin scattering due to the detuning of the three-wave coupling via a flow-induced Doppler shift in the IAW frequency. The important feature is the plateau that provides a more-favorable region for SBS growth, which moves outward toward the laser and lower electron plasma densities in time. The three curves (dashed, solid, dotted) correspond to the times 400, 600, and 800 ps after the start of the interaction pulse, respectively.

## 2. Modeling the Critical Surface

To relax the numerical constraints in the electromagnetic part of the problem, we previously used the paraxial approximation by setting  $\epsilon_{\text{par}} = 0$  in Eq. (3). This causes difficulty near the critical surface, however, since the local wave vector  $k_0(z)$  there is smaller and vanishes,  $k_0(z_t) = 0$ , at the turning point  $z = z_t$ , invalidating our approximation. One approach is to retain the second derivative in Eqs. (3) in a region surrounding the critical surface. We currently adopt a simpler method: Fig. 91.2 shows a typical simulation volume having its  $z$  axis

along the target normal and with the plasma density increasing with the axial coordinate due to target expansion. The length of the simulation box is chosen so that  $n_e(z = 0) \sim 0.1 n_c$  and  $n_e(L_z) \sim 0.7\text{--}0.8 n_c$ , which implies a standoff of approximately  $10 \mu\text{m}$  from the end of the simulation volume and the UV critical surface. Appropriate DPP boundary conditions must be provided for  $E_+$  at  $z = 0$  (see Fig. 91.3). The boundary conditions for  $E_-$  at  $z = L_z$  are obtained by treating the end of the simulation volume as a partially reflecting mirror by setting

$$E_-(\vec{x}_\perp, L_z) = \sqrt{R(t)} E_+(\vec{x}_\perp, L_z),$$



TC5980

Figure 91.2

The typical geometry used in simulating direct-drive LPI experiments. The solid target is assumed to have its outward normal along the  $z$  axis (pointing to the left), with the UV critical surface as indicated. The laser is incident from the left. The simulation volume is smaller than the envelope of the beam as indicated; DPP and SSD are modeled by applying the appropriate boundary condition (i.e., amplitude and phase) for the complex electric-field envelope  $E_+$  at  $z = 0$  (see Fig. 91.3). This gives rise to the characteristic speckle pattern in the box as it propagates to the end of the box at  $z = L_z$ . The region between  $z = L_z$  and the UV critical surface is not modeled in pF3D, but the reflection from the critical surface is accounted for by setting  $E_- = \sqrt{R} E_+$  at  $z = L_z$ , where  $R$  is the reflectivity arising from the stand-off region as calculated from the *SAGE* hydrodynamic profile. The envelope  $E_-$  then propagates backward through the box, exiting at  $z = 0$ , where the plasma reflectivity can be measured. Typically, the simulation volume is reduced to two dimensions with backward SBS present due to numerical constraints.

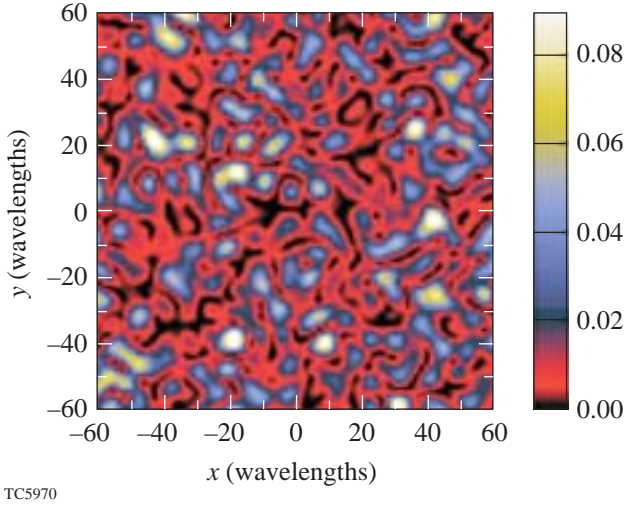


Figure 91.3

An example of the electric-field density, normalized to the average intensity, taken on the entrance plane of the box  $z = 0$ . This was created assuming the cylindrical top-hat model (in three dimensions)<sup>21</sup> corresponding to an  $f/6$  DPP.

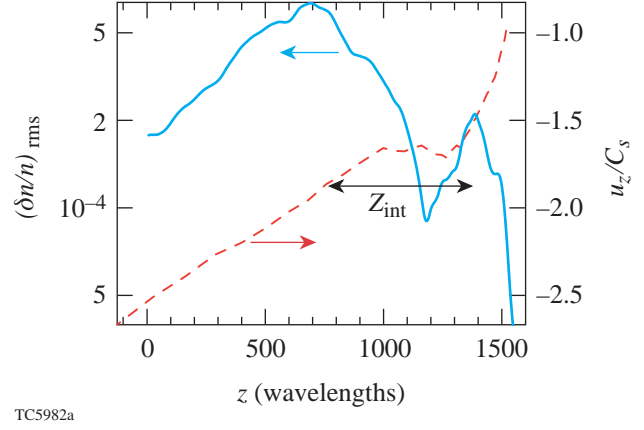


Figure 91.4

IAW amplitudes  $n_1$  [see Eq. (5)] averaged over the transverse extent of the simulation box, and plasma expansion velocity as a function of the axial coordinate  $z$ . Notice that there are two regions of significant IAW amplitude, one around the sonic point, where IAW's are resonantly driven by specularly reflected light, and the other corresponding to the shelf in plasma expansion velocity, where backward SBS gain is high.

with the reflectivity coefficient given by

$$R = \exp \left[ 2 \int_{L_z}^{z_t} \kappa_{ab}(z', t) dz' \right],$$

where  $\kappa_{ab} = v_{ei}/V_g$ . Typical values near the peak of the interaction pulse are  $R \sim 0.6$ . In this way, the electromagnetic (EM) backscatter seed has at least the proper intensity for the corresponding SAGE profile (if nonlinear interactions are negligible). The phase is not correct, although this is not expected to be important. Changes to this model will be made as our understanding regarding the nonlinear interactions near critical is improved. Angular and frequency broadening will be modeled if it is found to be important. We will incorporate a full-wave solver near the turning point if necessary.

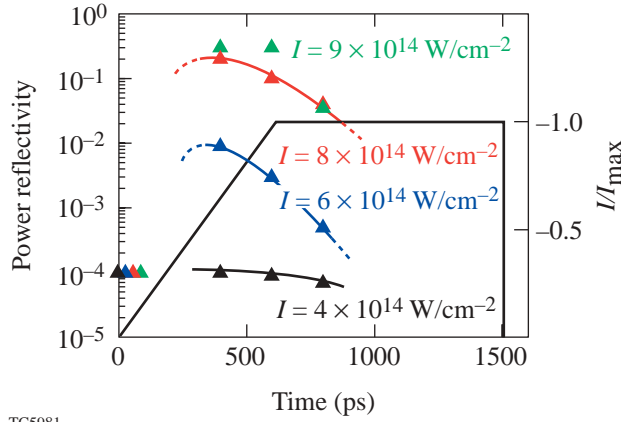
### 3. SBS Backscatter Signal in Simulation and Experiment

As in the experiment, simulations show a blue feature in the spectrum of backscattered light due to SBS coming from a flat region of expansion velocity. Indeed, examination of the plasma expansion velocity profile (Figs. 91.1 and 91.4) shows that there is a preferred location for SBS growth, the flat “shelf” of uniform velocity, which has a characteristic size of  $\sim 200 \mu\text{m}$ . In all other parts of the profile, the inhomogeneity scale length is short. This shelf is swept further downstream (toward the laser) with time, so that at later times the local

plasma density at the shelf falls rapidly (see Fig. 91.1). Based on an estimate of the expected SBS intensity gain in the shelf region, we may also be able to explain simply the early “quenching” of the SBS signal seen in the multibeam experiments.<sup>15</sup> Assuming the strong damping limit, and a uniform expansion velocity, the convective intensity gain in practical units is given by  $I_{\text{SBS}} = I_{\text{seed}} \exp(G)$ , with  $G = z_{\text{int}}/L_G$ , and

$$L_G^{-1} = 0.045 \frac{1}{v_i} \frac{\omega_0}{c} \frac{n_e/n_c}{\sqrt{1-n_e/n_c}} I_{15} \lambda_{\mu\text{m}} \frac{1}{T_{\text{keV}}}. \quad (8)$$

Taking  $z_{\text{int}}$  to be  $\sim 200 \mu\text{m}$  (as Fig. 91.1 shows to be the length of the shelf),  $v_{ia}/2k_0 C_a = 0.1$ ,  $I_{15} = 0.4$ ,  $\lambda_{\mu\text{m}} = 0.351$ , and  $T_{\text{keV}} = 2.2$ , we arrive at a gain  $G$  that as a function of the plasma density,  $G \sim 100(n_e/n_c)/\sqrt{1-n_e/n_c}$ , drops from a value of  $G = 30$  to 10 as the plasma density drops from  $n_e/n_c = 0.25$  to 0.1. This factor-of-3 reduction in the gain as the shelf moves to lower density (Fig. 91.1) explains why the SBS signal drops when the laser intensity is at its peak. This gain will be achieved after a time,  $\tau_{\text{SBS}}$  given approximately by  $\tau_{\text{SBS}} \sim G/v_{ia}(2k_0) < 30$  ps. Figure 91.5 shows actual power reflectivities, taken from recent pF3D simulations, at various times in the pulse (to gain a picture of the interaction over the whole laser pulse, some approximations have been made<sup>16</sup>).



TC5981

Figure 91.5

Laser power reflectivity, as a function of time, taken from simulations corresponding to a range of maximum average laser intensities between  $I = 4 \times 10^{14} \text{ W/cm}^2$  and  $I = 9 \times 10^{14} \text{ W/cm}^2$ . The laser pulse was turned on at  $t = 0$  and then ramped linearly to maximum intensity in 500 ps after which it was held fixed for an additional 1 ns, as in typical OMEGA experiments. Notice that the reflectivity peaks early in the pulse.

Currently we are investigating the more complicated, and less easily predicted, effects of EM seeding from the critical surface and the effects of multiple-beam irradiation and quantifying the ability of SSD bandwidth to suppress SBS.

**a. EM seeding of backward SBS.** The EM seeding of Brillouin backscatter in the strongly underdense region is affected by the plasma inhomogeneity. Each frequency component of the backscattered light can be resonant with ion waves only in a spatially narrow region such that the frequency-matching conditions are satisfied locally and  $\omega_0 - \omega_1 = \omega_{\text{IAW}}[1 - M_{\parallel}(z)]$ , where  $\omega_1$  is the frequency of the backscattered radiation and  $\omega_{\text{IAW}} = |\mathbf{k}_{\text{IAW}}|C_a$  is the IAW frequency for a sound wave with wave number  $\mathbf{k}_{\text{IAW}}$ . The spatial extent of this resonance region is determined by the width of the ion-acoustic resonance  $\sim v_{\text{ia}}^{-1}$  and the scale length of the flow Mach number  $\mathbf{M}$ . The wave-number-matching conditions  $\mathbf{k}_0 = \mathbf{k}_1 + \mathbf{k}_{\text{IAW}}$  are determined by the scattering geometry only since the magnitude of the wave vector of scattered light is essentially unchanged,  $|\mathbf{k}_1| \approx |\mathbf{k}_0| = \omega_0/c\sqrt{1 - n_e/n_c}$ , because the shift by the ion-acoustic frequency  $\omega_0 - \omega_1$  is very small compared to  $\omega_0$ .

It has been suggested that the sonic point is of special importance because light specularly reflected by the critical surface with little or no spectral shift<sup>17</sup> will be resonant with the IAW at this point and may drive them to large amplitude.

This effect is evident in Fig. 91.4. The resonance may be less important, however, if the reflected light is not monochromatic and is spread in angle and frequency due to nonlinear interactions near the critical surface. In addition, experimental evidence indicates that the absorption is much greater than predicted by Eq. (10), and the backscattering seed at the sonic point may be substantially less than is shown in Fig. 91.4. We would not expect specularly reflected light to provide an efficient seed for SBS occurring in the supersonic region due to the large frequency mismatch.

In summary, the parametric reflections from other beams (in multibeam geometries) are expected to be more important than specular reflection for seeding the blue part of the scattered light spectrum, and there is much experimental evidence for synergy between the beams, while interactions near the sonic point are influenced by both specular and parametric reflections in both single and multibeam geometries. The region near the critical surface associated with the red feature in the spectrum of reflected light is the most complicated and best investigated with a code capable of solving the full wave equation.

**b. Anomalous absorption.** In the absence of parametric reflections, at low intensity, one would expect the laser absorption  $\eta$  to be due to classical inverse Bremsstrahlung only. Integrating the equations for laser intensity [obtained from Eq. (3)],

$$\frac{\partial}{\partial z} (V_g |E_{\pm}|^2) = \mp \frac{v_{ei}}{V_g} (V_g |E_{\pm}|^2), \quad (9)$$

over *SAGE* density and temperature profiles, one obtains the reflectivity  $R = 1 - \eta$ , where

$$R = \exp \left[ -2 \int_0^{z_t} \kappa_{ab}(z') dz' \right], \quad (10)$$

$\kappa_{ab} = v_{ei}/V_g$  is a function that depends on the density and temperature, and  $z_t$  is the turning point for the transverse waves, defined by  $1 - n_e(z_t)/n_c - \sin^2(\theta) = 0$ . For a *SAGE* profile at  $t = 400$  ps, the above formula predicts  $R = 0.025$  (for  $\theta = 0^\circ$ ). This lower bound on the reflectivity is larger than the experimentally observed reflectivity by approximately two orders of magnitude.

Possible explanations for this serious discrepancy include inaccuracies in the *SAGE* profiles near the critical surface, where most of the absorption occurs, and where it is especially sensitive to temperature through the electron-ion collision frequency,

$$v_{ei} \sim 8.16 \frac{\ln \Lambda}{10} Z_{\text{eff}} \frac{n_e}{n_c} \left( \frac{0.351}{\lambda_{0,\mu\text{m}}} \right)^2 T_{e,\text{keV}}^{-3/2} \text{ps}^{-1}, \quad (11)$$

a factor that appears in the exponent of the equation for the reflectivity, Eq. (10). Other possible explanations are the geometric effect of diffuse scattering through a rough critical surface (although a scattering into  $2\pi$  radians would be required, and this can be ruled out experimentally) and increased collisionality brought about by ion turbulence. A close investigation of the backscatter spectrum, together with pF3D simulations, might be the best route to resolving this outstanding problem and offers the possibility of providing a diagnostic for laser absorption.

#### 4. Self-Focusing Instability and Self-Smoothing

Another area where pF3D simulations are expected to provide insight is the investigation of so-called plasma-induced self-smoothing of laser light. This is a mechanism in which the spatial and temporal correlation length of the laser can be dramatically reduced, as a result of nonlinear plasma response related to the self-focusing (SF) instability and forward SBS. Although this is presently a very active area of research, with strong experimental evidence showing its importance to backward SBS in underdense plasmas,<sup>18–20</sup> effects likely of importance to direct drive such as laser imprint and saturation of TPD have not been investigated either experimentally or theoretically (including through simulation).

The onset of self-smoothing is related to the SF instability and has a threshold which, in practical units, is given by

$$p \sim 0.39 \frac{I_{15} \lambda_{\mu\text{m}}^2}{T_{e,\text{keV}}} f_{\#}^2 \left( \frac{n_e}{n_c} \right) > 1, \quad (12)$$

where the factor of order unity (0.39 here) comes from assuming a cylindrical top-hat DPP (distributed phase plate) spectrum in 3-D.<sup>21</sup> For relevant parameters, it is seen that SF might become important at higher intensities, nearing  $1 \times 10^{15} \text{ W/cm}^2$ . This is demonstrated in Fig. 91.6, which shows

a longitudinal slice of the electric-field intensity of a DPP beam. Notice the reduction in the size of the laser speckle pattern, which is also associated with a reduction in the laser coherence time.

The increased incoherence of the laser beam can disrupt and reduce the level of coherent parametric instabilities, which is beneficial for inertial confinement fusion (ICF). Regarding SBS, the shelf in the expansion velocity makes the OMEGA experiments quite different from previous investigations of SBS in inhomogeneous plasmas, where there was no preferential region for growth. Competition between self-smoothing and SBS can be revealed by the spatial location of SBS ion waves, as reported for LULI experiments using a Thomson-scattering diagnostic.<sup>18</sup> A close examination of

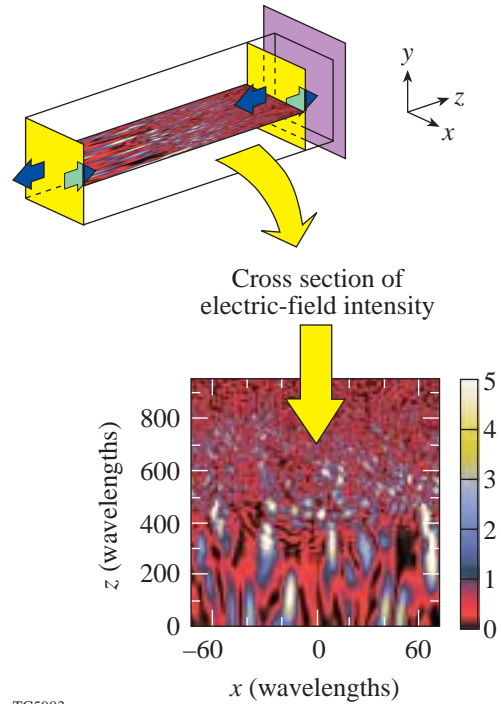


Figure 91.6

At laser intensities nearing  $I = 1 \times 10^{15} \text{ W/cm}^2$ , the threshold for the self-focusing instability [Eq. (12)] is exceeded in the intense laser speckles. This leads to a reduction in the transverse correlation length of the laser light and frequency broadening. This effect, which has become known as plasma self-induced smoothing, could have an impact on parametric processes such as the two-plasmon-decay instability. This figure illustrates this by showing a longitudinal cross section of the laser intensity (in real space), normalized to the average intensity. The light propagates along the  $z$  axis, from bottom to top in the figure. The quarter-critical surface is just beyond the region where the self-smoothing has set in. This could have a saturating effect on the two-plasmon-decay instability.

the SBS signal at high laser intensity may then give valuable information on self-smoothing. This is of broad significance because the incoherence generated by filament instability that is responsible for self-smoothing will affect all resonant parametric processes.

Self-smoothing could have important consequences for the TPD instability since the observed behavior of TPD electrons seems to suggest saturation near  $10^{15}$  W/cm<sup>2</sup>, which is similar to the threshold of SF. The TPD instability, as inferred from fast electrons, is also dependent on SSD bandwidth. This dependence seems consistent with a reduction of filamentation at higher SSD bandwidth. The addition of SSD bandwidth is assumed to suppress SF/filamentation,<sup>22,23</sup> but this has not been studied in the present context.

### Discussion

We began by discussing the importance of large-scale simulations in the interpretation and understanding of LPI in ICF fusion experiments and the differences between the indirect- and direct-drive approaches. We also outlined the difficulties and challenges that these types of simulations present and indicated that LPI in direct-drive plasmas has received comparatively little attention. We have set out to remedy this situation and have, in collaboration with LLNL, begun to modify the interaction code pF3D for use in modeling direct-drive plasmas.

The first pF3D results of backward SBS scattering using a realistic inhomogeneous plasma profile, as predicted by the code *SAGE* for recent LPI interaction experiments, have been presented. These simulation results have been used to interpret the experimental backscatter data and have reproduced the behavior of the blue spectral feature observed. Future work will carefully examine the effect of SSD bandwidth and polarization smoothing.

The narrow region near critical is currently treated in a rather simple way. This region is being studied with a separate code for solving the full wave equation. These two codes could be integrated in the future if necessary.

A large discrepancy was found in the level of absorption due to inverse bremsstrahlung between that calculated from *SAGE* and the value obtained experimentally. The level of ion-acoustic fluctuations near the sonic point is dependent on the plasma reflectivity and may potentially be used as a diagnostic for absorption. The pF3D code may be used in conjunction with experiments to resolve this problem.

Finally, it was demonstrated that self-smoothing will become important at higher laser intensities, which will impact all parametric processes including SBS, SRS, and TPD. It will also modify the laser imprint. Due to the potential importance of all these processes, the newly modified pF3D will be used to address these issues in the very near future.

### ACKNOWLEDGMENT

This work was supported by the U.S. Department of Energy Office of Inertial Confinement Fusion under Cooperative Agreement No. DE-FC03-92SF19460 and the University of Rochester. The support of DOE does not constitute an endorsement by DOE of the views expressed in this article. The author also thanks C. H. Still and R. L. Berger for their assistance.

### REFERENCES

1. J. D. Lindl, *Phys. Plasmas* **2**, 3933 (1995).
2. E. J. Valeo and K. G. Estabrook, *Phys. Rev. Lett.* **34**, 1008 (1975).
3. R. L. Berger *et al.*, *Phys. Plasmas* **5**, 4337 (1998).
4. J. Myatt, D. Pesme, S. Huller, A. Maximov, W. Rozmus, and C. E. Capjack, *Phys. Rev. Lett.* **87**, 255003 (2001).
5. V. V. Eliseev *et al.*, *Phys. Plasmas* **3**, 3754 (1996).
6. S. Huller, Ph. Mounaix, and V. T. Tikhonchuk, *Phys. Plasmas* **5**, 2706 (1998).
7. D. Pesme, presented at the LLNL Workshop on Saturation of Simulated Raman and Brillouin Instabilities, Livermore, CA, 3–5 April 2002.
8. H. A. Rose, *Phys. Plasmas* **4**, 437 (1997).
9. H. A. Rose, *Phys. Plasmas* **3**, 1709 (1996).
10. L. Divol *et al.*, *Bull. Am. Phys. Soc.* **46**, 293 (2001).
11. A. Maximov, Laboratory for Laser Energetics, private communication (2001).
12. H. A. Rose, *Phys. Plasmas* **3**, 1709 (1996).
13. R. S. Craxton and R. L. McCrory, *J. Appl. Phys.* **56**, 108 (1984).
14. V. T. Tikhonchuk, J. Fuchs, C. Labaune, S. Depierreaux, S. Huller, J. Myatt, and H. A. Baldis, *Phys. Plasmas* **8**, 1636 (2001).
15. Laboratory for Laser Energetics LLE Review **87**, 128, NTIS document No. DOE/SF/19460-397 (2001). Copies may be obtained from the National Technical Information Service, Springfield, VA 22161.
16. We have adopted the following methodology that assumes that there are no correlations that live longer than several tens of picoseconds. To put this in perspective, the damping time of an ion wave with wave number given by  $2\omega_0/c$  is approximately 1 ps, and only ten times larger for forward SBS at 5°. The time for SBS to reach its asymptotic state,  $\tau_{\text{SBS}}$  can be crudely approximated as  $\tau_{\text{SBS}} \sim G/v_{\text{ia}}(2k_0)$ , which is less than 10 ps. At the chosen starting time the

hydrodynamic profile is initialized with *SAGE* and the laser turned over a few picoseconds to the appropriate intensity. When an asymptotic state is reached, the SBS is expected to be representative of that occurring.

17. The linear phase modulation due the motion of the critical surface imparts a negligible frequency shift.
18. C. Labaune, presented at the LLNL Workshop on Saturation of Simulated Raman and Brillouin Instabilities, Livermore, CA.
19. A. J. Schmitt and B. B. Afeyan, *Phys. Plasmas* **5**, 503 (1998).
20. A. V. Maximov *et al.*, *Phys. Plasmas* **8**, 1319 (2001).
21. H. A. Rose, *Phys. Plasmas* **2**, 2216 (1995).
22. R. L. Berger *et al.*, *Phys. Rev. Lett.* **75**, 1078 (1995).
23. R. L. Berger *et al.*, *Phys. Plasmas* **6**, 1043 (1999).